

Constraints on the galaxy “main sequence” at $z > 5$: the stellar mass of HDF850.1

Stephen Serjeant¹ and Lucia Marchetti¹

¹*Department of Physical Sciences, The Open University, Milton Keynes, MK7 6AA, UK*

Received 2013

ABSTRACT

We present rest-frame optical and near-infrared detections of one of the highest redshift submm-selected galaxies to date, HDF850.1. We do not detect the previously proposed counterpart HDF850.1K in new deep J and H -band *HST* WFC3 data, placing a strong limit of $H - K > 3.8$, concluding that the K -band source is spurious. However, we detect $5.8\ \mu\text{m}$ and $8\ \mu\text{m}$ emission co-located with the submm in deblended images. After modelling and removing the flux contributions from another foreground galaxy, we constrain the stellar mass of HDF850.1 to be $(2.5 \pm 1)\mu^{-1} \times 10^{11} M_{\odot}$ for a lensing magnification $\mu = 1.9 \pm 0.3$, with a specific star formation rate of $8.5\ \text{Gyr}^{-1}$, faster than the $1 - 4\ \text{Gyr}^{-1}$ observed for UV -selected galaxies at this epoch.

Key words: cosmology: observations - galaxies: evolution - galaxies: formation - galaxies: star-burst - infrared: galaxies - submillimetre

1 INTRODUCTION

HDF850.1 was the first galaxy discovered in a blank field submm-wave survey (Hughes et al. 1998), proving the feasibility of blank-field sky surveys at submm wavelengths. Together with the earlier discoveries of submm galaxies detected with the help of strong gravitational lens magnification by foreground galaxy clusters (Smail et al. 1997) and that of submm galaxies in other pioneering blank-field surveys (e.g. Barger et al. 1998), this new population or category of high-redshift ultraluminous starbursts ushered in a new era of extragalactic survey astronomy and helped establish some of the first observational evidence for galaxy downsizing. Despite this, even today it remains unclear why so few $z > 4$ submm galaxies have been discovered. For example, it is not clear whether further populations of more extreme but rarer starbursts await discovery at $z > 4$ with e.g. extremely red submm colours in *Herschel* SPIRE data (e.g. Pope & Chary 2010), or whether the median $z = 2.4$ for submm galaxies (e.g. Swinbank et al. 2004) holds at all luminosities, marking the peak epoch of stellar mass assembly for all sufficiently massive galaxies.

HDF850.1 itself nonetheless proved an unusually hard target for multi-wavelength follow-ups, despite intensive multiwavelength campaigns in the field (e.g. Serjeant et al. 1997, Hogg et al. 1997, Downes et al. 1999, Aussel et al. 1999, Garrett et al. 2000, Brandt et al. 2001, Alexander et al. 2003, Capak et al. 2004, Morrison et al. 2010, Conselice et al. 2011, Teplitz et al. 2011, Oliver et al. 2012, Guidetti et al. 2013, Teplitz et al. 2013). Dunlop et al. (2004) noted the high likelihood association with the $z \simeq 1$ elliptical 3-

586.0 ($p \simeq 0.05$, Fig. 1), but also that this association disagreed with an IRAM 1.3 mm interferometric position. The proximity of the foreground elliptical makes gravitational lensing a significant consideration. Dunlop et al. performed careful subtraction of the foreground elliptical in *Subaru* K -band data, finding a faint $K \simeq 23.5$ counterpart, tentatively also detected in *HST* NICMOS H -band data with $H - K = 1.4 \pm 0.35$. However it transpired that the position of this K -band source did not agree with subsequent SMA 345 GHz imaging by Cowie et al. (2009), nor with tentative VLA detections. Cowie et al. further state that HDF850.1 therefore “has no detectable optical or NIR light”, and their submm/radio photometric redshift estimate placed this objects at $z = 4.1 \pm 0.5$ making it potentially one of the highest redshift submm galaxies.

The advent of the *Herschel* Space Observatory then brought many major milestones in the study of high- z submm galaxies: SPIRE’s very high survey mapping efficiency (Griffin et al. 2010) made possible many successful and much larger blank-field surveys (e.g. Eales et al. 2010, Oliver et al. 2012); millimetric and submm spectroscopy of these bright submm galaxies easily yielded redshifts directly from CO lines, without recourse to multi-wavelength identifications (e.g. Lupu et al. 2012, Frayer et al. 2011); and the steep submm source counts were confirmed to generate a strong gravitational lens magnification bias, demonstrating that submm surveys are extremely efficient at finding strong gravitational lenses (e.g. Negrello et al. 2010).

Following this, and over a decade after the original discovery of HDF850.1, Walter et al. (2012) made a break-

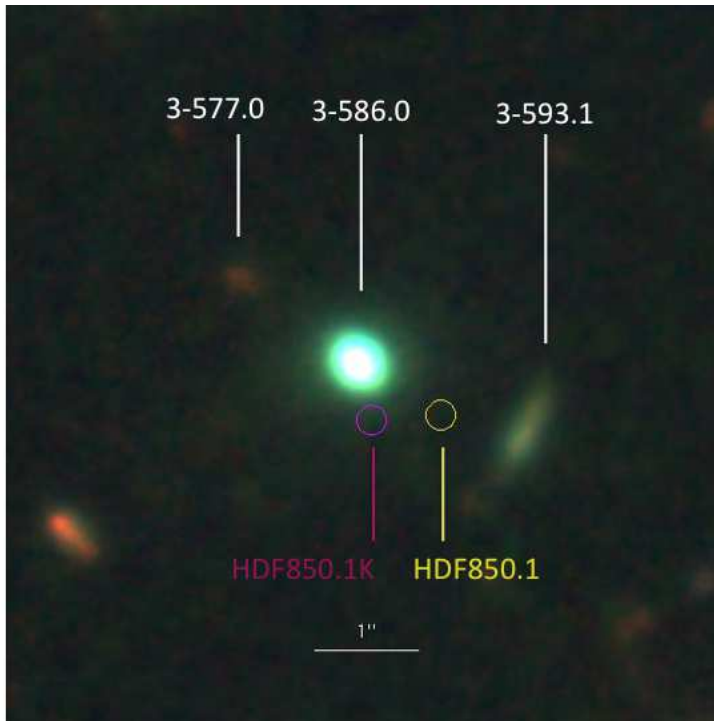


Figure 1. *HST* composite colour image of the HDF850.1 system centred on 3-586.0, with I_{F814W} -band data in blue, J_{F125W} -band in green, and H_{F160W} -band in red. Named galaxies are marked. The position of HDF850.1K is from Dunlop et al. (2004), while HDF850.1 is shown at the position of the [CII] emission from Walter et al. (2012). North is up and East to the left. Note that the $z = 1.224$ foreground elliptical 3-586.0 appears relatively blue in the near-infrared.

through CO and [CII] redshift determination of HDF850.1. This placed the system at $z = 5.183$, making it one of the highest confirmed redshift of any submm galaxy together with, e.g., the $z = 5.2$ lensed submm galaxy identified by Combes et al. 2012 and the $z = 6.34$ starburst discovered by Riechers et. al 2013. Remarkably HDF850.1 remained nonetheless undetected in all rest-frame ultraviolet, optical and near-infrared data, making it appear completely obscured despite the moderate surface density of its star formation ($\sim 35 M_{\odot} \text{ yr}^{-1} \text{ kpc}^{-2}$, uncertainty $\sim 50\%$; Walter et al. 2012).

In this paper we use new *HST* WFC3 archival near-infrared data, plus a careful re-analysis of the archival *Spitzer* data, to reassess these claimed optical/near-infrared non-detections as well as the claimed magnification factors in this lensed system; our key results are the first rest-frame optical/near-infrared detections of HDF850.1. Section 2 presents our observational data. The photometric data and the gravitational lens system as a whole are modelled in section 3. In section 4 we discuss the implications and context of our results, and we conclude in section 5. Throughout this paper, we refer to the submm source as HDF850.1 and the *K*-band source from Dunlop et al. (2004) as HDF850.1K. We adopt a concordance cosmology, with a Hubble constant $H_0 = 72 \text{ km s}^{-1} \text{ Mpc}^{-1}$ and density parameters $\Omega_M = 0.3$, $\Omega_{\Lambda} = 0.7$.

2 OBSERVATIONAL DATA

2.1 *HST* near-infrared imaging

The GOODS-N field, among other fields, has recently been observed with the Wide Field Camera 3 (WFC3) on the *HST* under the CANDELS survey (Grogin et al. 2011, Koekoemoer et al. 2011; program 12443, PI: Faber). We performed a noise-weighted coadd of all available pipeline-processed data on HDF850.1 in the F125W (*J*-band) and F160W (*H*-band) filters and registered the coadded images to the HDF-N frame. The total exposure time is 10.0 hours in F160W and 8.9 hours in F125W, and the data were taken between 31 March 2012 and 7 November 2012.

We modelled the foreground lensing galaxy, 3-586.0, with the GALFIT package (Peng et al. 2010a). Our approach in modelling the lens is to use the *smallest* number of components possible, i.e. keeping the model as simple as possible. The objective is a purely phenomenological description of this galaxy for the purposes of subtracting its flux. At 814 nm, the lens is modelled as the sum of two Sérsic profiles, though allowing five Fourier distortions of the smaller profile. Galaxies 3-577.0 and 3-593.1 were additionally modelled, the latter incorporating a bending mode. At $1.25 \mu\text{m}$ and $1.6 \mu\text{m}$ the Fourier distortions to the smaller Sérsic profile were not found to be necessary but an addition central point spread function was incorporated.

Fig. 2 shows the lens-subtracted *J*-band and *H*-band data. The tentative *H*-band counterpart seen in shallower NICMOS data by Dunlop et al. (2004) is not seen in this new data. To quantify the constraint, we performed $0.4''$ diameter aperture photometry (which we then aperture cor-

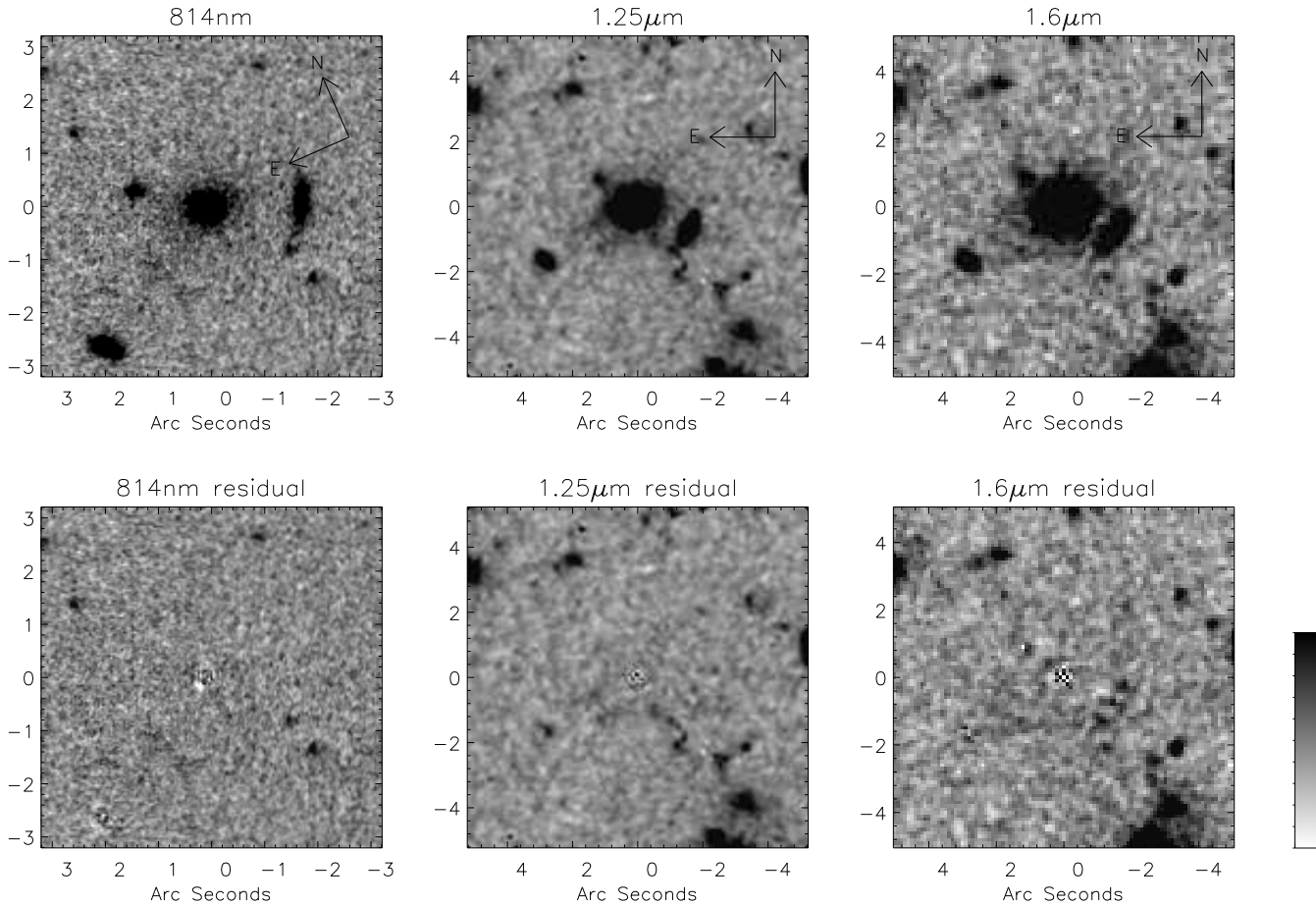


Figure 2. *HST* lens-subtracted imaging of HDF850.1 with the WFC2 I_{F814W} -band (left), WFC3 J_{F125W} -band (centre) and WFC3 H_{F160W} -band (right). The top row shows the unsubtracted imaging, while the bottom row give the residuals after subtracting out 3-577.0, 3-586.0 and 3-593.1 (Fig. 1). Neither the submm source from Walter et al. (2012) nor the K-band source from Dunlop et al. (2004) are detected in the residuals. The plot limits are approximately $\pm 5.0\sigma$, $\pm 7.4\sigma$ and $\pm 4.9\sigma$ at 814 nm, $1.25\ \mu\text{m}$ and $1.6\ \mu\text{m}$ respectively, where σ is the pixel noise level in each case. As with all greyscale figures in this paper, the scaling is linear, and a linear greyscale sidebar is shown for this figure only.

	J_{F125W}	H_{F160W}	$5.8\ \mu\text{m}/\mu\text{Jy}$	$8\ \mu\text{m}/\mu\text{Jy}$
3-586.0	21.24 ± 0.05	20.34 ± 0.05	8.25 ± 0.40	6.88 ± 0.49
HDF850.1	< 28.2	< 27.3	2.72 ± 0.53	5.93 ± 0.69
HDF850.1K	< 28.5	< 27.3	–	–
3-593.1	23.62 ± 0.15	23.13 ± 0.15	2.97 ± 0.39	2.87 ± 0.49

Table 1. New photometry of the four nearest galaxies in the HDF850.1 field. Magnitudes are in the Vega system. Upper limits are 2σ in an $0.4''$ diameter aperture, corrected to total flux assuming a point source; J - and H -band detections use a $3''$ diameter aperture. The 3-583.0 photometric detections on the J - and H -band images are consistent within 1σ with photometry of the GALFIT model image; the GALFIT image measurements are quoted here, since they exclude neighbouring galaxies. The 3-593.1 J - and H -band measurements were made on images with the GALFIT 3-586.0 model subtracted. IRAC fluxes are from the point source fitting discussed in the text.

rected to total flux assuming a point source) at locations at approximately the same radial distance from the lens, then calculated the standard deviation of these measurements. The 2σ upper limits at the location of the [CII] emission is $J < 28.2$ and $H < 27.3$, and at the location of HDF850.1K the limits are $J < 28.8$ and $H < 27.3$. Our H -band pho-

tometry of the foreground lensing galaxy 3-586.0 (table 1) is consistent with the Dunlop et al. (2004) H -band measurement of 20.40 ± 0.05 . Table 1 lists our new photometry for the galaxies in this system. Our $H - K > 3.8$ colour for HDF850.1K (equivalent to $H_{AB} - K_{AB} > 3.3$) contrasts

with the $H - K = 1.4$ measurement in Dunlop et al. (2004) from their tentative NICMOS detection.

As a further simple test of the lens subtraction, we attempted inserting a simulated source at the same radial distance from the lens as HDF850.1K, using a single Sérsic profile lens model in order to demonstrate the robustness of the lens modelling. Accordingly, we rescaled the H -band image by a factor of $1/63$, equivalent to the reported H -band flux ratio of the lens and HDF850.1K in Dunlop et al. (2004), offset the rescaled image, added it to the H -band image, and finally re-performed the lens subtraction. The offset was performed in a different direction to the HDF850.1K-lens offset, but with the same magnitude. The result is shown in Fig. 3. Note the clear detection of the simulated counterpart. We conclude that if the tentative H -band NICMOS detection were real, it should easily have been reproduced in our data.

2.2 *Spitzer* near-infrared imaging

HDF850.1 was observed as part of the Great Observatories Origins Deep Program (GOODS) in 2004 (Dickinson et al. 2003) using the Infrared Array Camera (IRAC) and the Multiband Imaging Photometer for SIRTf (MIPS). In this paper we will deal only with the IRAC GOODS data, because the MIPS resolution is too poor to resolve the system. The *Spitzer* IRAC data were taken at two epochs. The fortunate central location of HDF850.1 within GOODS led to its being observed in both epochs. We registered the data from both epochs separately to galaxies local to HDF850.1 in the I_{F814W} -band *HST* WFPC2 data.

The close proximity of HDF850.1 to several foreground galaxies (Fig. 1) complicates the *Spitzer* photometry of HDF850.1 (e.g. Cowie et al. 2009). Further complicating the analysis is the anisotropic point spread function, particularly at the shorter wavelengths. The effective radius of the foreground lens 3-586.0 is much smaller than that of an IRAC pixel, so opted to treat the lens as a point source for *Spitzer*, in keeping with our philosophy to use models with only just sufficient complexity to characterise the lens. We used a 5×5 oversampled point spread function in each epoch to construct the model profile of the foreground lens at $5.8 \mu\text{m}$ and $8 \mu\text{m}$. The lens-subtracted images were rebinned to the same scale and coadded, and the coadded $5.8 \mu\text{m}$ and $8 \mu\text{m}$ data is shown in Fig. 4. As this adequately subtracted the lens we did not attempt more elaborate lens modelling. An excess emission to the South-West of 3-586.0 is clearly visible in both channels, as well as in the separate epochs (not shown). Furthermore, the centroid of this emission is clearly not consistent with flux solely from the neighbouring foreground galaxy 3-593.1. In section 3.2 we will model the SED of 3-593.1 to assess the likely contribution from this galaxy to the *Spitzer* flux. Fig. 4 makes it immediately clear that the cause of the previous non-detection of HDF850.1 is not heavy obscuration in the submm galaxy (c.f. Walter et al. 2012), but rather the blending from foreground systems. (HDF850.1 may nonetheless still be heavily obscured.)

The positions of all the galaxies are known, and given that the data is already inconsistent with flux at only 3-586.0 and 3-593.1, we tried a three-component fit to the $5.8 \mu\text{m}$ and $8 \mu\text{m}$ images, with point sources fixed at the locations of 3-586.0, 3-593.1 and the submm emission. As before, the PSF subtraction was performed separately on

	3-586.0	HDF850.1	3-593.1
3-586.0	0.0023	-0.0066	0.0018
HDF850.1	-0.0066	0.038	-0.018
3-593.1	0.0018	-0.018	0.018

Table 2. Covariance matrix for the $5.8 \mu\text{m}$ fluxes normalised to the maximum-likelihood values, i.e. $\text{Cov}(x_1, x_2)/(\mu_1 \mu_2)$ where x_1 and x_2 are the variables being compared, and μ_1 and μ_2 are their maximum likelihood fluxes. The maximum-likelihood values themselves are given in table 1.

	3-586.0	HDF850.1	3-593.1
3-586.0	0.0051	-0.0064	0.0052
HDF850.1	-0.0064	0.014	-0.015
3-593.1	0.005	-0.015	0.030

Table 3. Covariance matrix for the $8 \mu\text{m}$ fluxes normalised to the maximum-likelihood values, i.e. $\text{Cov}(x_1, x_2)/(\mu_1 \mu_2)$ where x_1 and x_2 are the variables being compared, and μ_1 and μ_2 are their maximum likelihood fluxes. The maximum-likelihood values themselves are given in table 1.

the two epochs, though the epochs were constrained to have the same fluxes and source positions in the modelling. We detected the submm source at 8.3σ at $8 \mu\text{m}$, and 5.1σ at $5.8 \mu\text{m}$. The photometric measurements are given in table 1. The measured fluxes of the submm source are anticorrelated with the foreground galaxies; covariance matrices are given in tables 2 and 3. At both wavelengths and both epochs, the residuals are consistent with blank fields. It is not possible with this data to separate the IRAC fluxes of HDF850.1 and HDF850.1K; we will return to the reality of HDF850.1K in section 4.

The lens subtraction at $3.6 \mu\text{m}$ and $4.5 \mu\text{m}$ is much more complicated due to the highly anisotropic point spread function that varies across the detectors. Furthermore, there is a less favourable contrast ratio of the background sources against the foreground lens. We nonetheless attempted to model the net PSF using the TINYTIM software (Krist et al. 2011), using the GOODS-N *Spitzer* coverage maps to estimate the distribution of detector pixel locations for the lens at each epoch. Reasonably acceptable fits were found to be possible using the $1.6 \mu\text{m}$ GALFIT solution as a starting point. Fig. 5 shows the two epochs at $3.6 \mu\text{m}$ and $4.5 \mu\text{m}$. We found that the residuals depend sensitively on the assumed point spread function and the lens model components, so for the purposes of constraining the flux at the position of the submm galaxy these data are less useful than the longer wavelength IRAC channels, despite the larger PSFs at longer wavelengths, because the longer-wavelength PSFs are less asymmetrical. We therefore conservatively opt not to use the $3.6 \mu\text{m}$ and $4.5 \mu\text{m}$ data to constrain the fluxes of the submm galaxy. Nevertheless, the approximate combined fluxes of HDF850.1 and 3-593.1 of $\sim 2.6 \mu\text{Jy}$ and $\sim 2.9 \mu\text{Jy}$ at $3.6 \mu\text{m}$ and $4.5 \mu\text{m}$ respectively are consistent with our SED fits to the individual galaxies discussed below, which yield totals of $1.7 \mu\text{Jy}$ and $3.0 \mu\text{Jy}$ respectively.

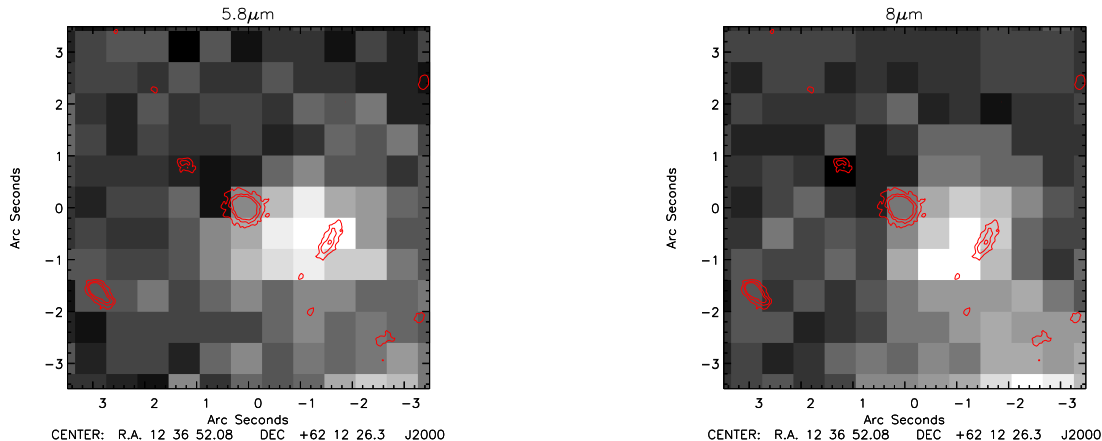


Figure 4. *Spitzer* lens-subtracted $5.8\mu\text{m}$ and $8\mu\text{m}$ images. North is up and East to the left. The foreground elliptical 3-586.0 was subtracted separately in the two epochs of *Spitzer* data, which were then combined. The red contours trace the I_{F814W} -band *HST* WFPC2 data. Note that the *Spitzer* residual is not consistent with emission solely from the location of the foreground galaxy 3-593.1 (Fig. 1). The $5.8\mu\text{m}$ image is scaled from approximately -2.6σ to 8.5σ , while the $8\mu\text{m}$ image is scaled from approximately -3.9σ to 12.9σ where in each case σ is the pixel noise level.

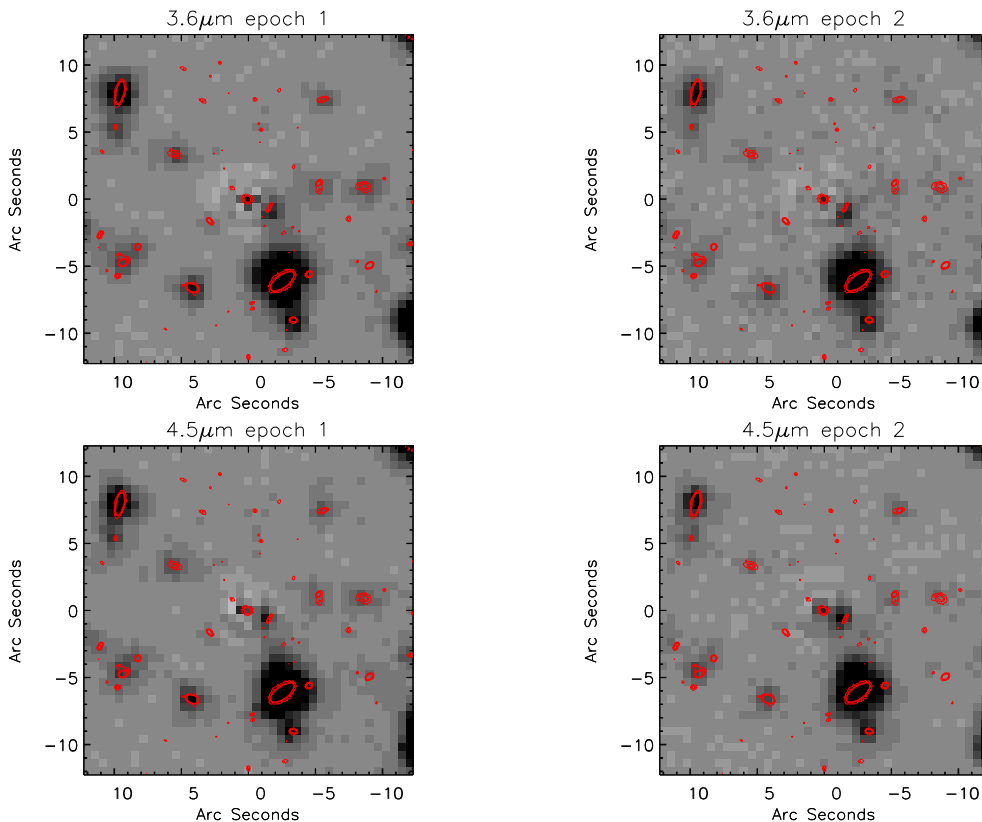


Figure 5. *Spitzer* lens-subtracted $3.6\mu\text{m}$ and $4.5\mu\text{m}$ images. The extended component of the foreground elliptical 3-586.0 (only slightly extended at this pixel scale) has been subtracted, but the other components have been left. There is evidence for a central residual point source in the lens. The red contours trace the I_{F814W} -band *HST* WFPC2 data. The greyscales are scaled show approximately $\pm 28\sigma$ where σ is the pixel noise level.

3 MODELLING

3.1 Gravitational lens modelling

Both HDF850.1 and HDF850.1K have been argued to be only moderately lensed by the foreground $z = 1.224$ ellip-

tical galaxy 3-586.0. In this section we critically re-assess these claims.

We adopt a Singular Isothermal Ellipsoid (SIE) model for the foreground lens, because in the image plane at the locations of HDF850.1 and HDF850.1K, there are only very small differences between the SIE model and a compos-

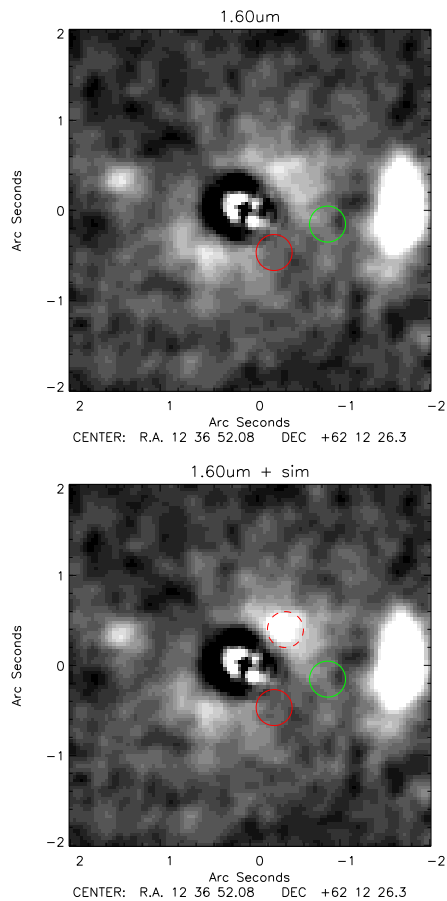


Figure 3. *HST* lens-subtracted WFC3 H_{F160W} -band data (top) with a *maximally simple* lens model of a single Sérsic profile. The image pixels are oversampled in these images for clarity of presentation, though this accentuates residuals in the image centre, due to the sensitivity to the modelling of the PSF on scales significantly smaller than a detector pixel. Note the faint diffuse residual flux. In the bottom panel, a simulated source has been inserted at the location of the dashed red circle, with the reported H -band flux from Dunlop et al. (2004). The green circle marks the position of the submm [CII] emission in Walter et al. (2012), while the red circle marks the location of the proposed K -band identification from Dunlop et al. (2004). If there were an H -band source at the location of HDF850.1K with the previously reported H -band flux, it would have been easily detectable in this image, even in this minimally-complex subtraction, so the non-detection is unlikely to be an artefact of our lens galaxy modelling.

ite Navarro-Frenk-White profile plus de Vaucouleurs’ profile (e.g. Gavazzi et al. 2007). The SIE model has a critical radius θ_{crit} defined as

$$\left(\frac{\theta_{\text{crit}}}{1''}\right) = \left(\frac{\sigma}{186 \text{ km s}^{-1}}\right)^2 \left(\frac{D_{\text{LS}}}{D_{\text{S}}}\right) \quad (1)$$

where D_{LS} and D_{S} are the angular diameter distances between lens and source and between observer and source respectively, and σ is the velocity dispersion. In our adopted cosmology, the source redshift of $z_{\text{s}} = 5.183$ and lens redshift $z_{\text{l}} = 1.224$ imply $D_{\text{S}} = 1238.3 \text{ Mpc}$ and $D_{\text{LS}} = 638.0 \text{ Mpc}$. The model also has an ellipticity, the magnitude and direction of which is determined by the *HST F814W*-band imag-

ing (Dunlop et al. 2004) to be $e = 0.22$, position angle 44.2° East of North.

To constrain the velocity dispersion σ , we use two approaches. Firstly, di Serego Alighieri et al. (2005) present rest-frame B -band fundamental plane observations of 18 $z \simeq 1$ early-type galaxies from the K20 survey. Applied to the *HST F814W* data on 3-586.0, their best fit model predicts $\sigma = 129 \text{ km s}^{-1}$, and the dispersion of their data around their best fit model implies an uncertainty in this prediction of $\pm 39 \text{ km s}^{-1}$. Secondly, Holden et al. (2005) present observations of four early-type galaxies at $z = 1.237$, almost exactly the same redshift as our lensing galaxy 3-586.0. Scaling from each of these galaxies assuming $\sigma^{1.2} \propto r_{\text{eff}} I_{\text{eff}}^{0.83}$ (where r_{eff} and I_{eff} are the effective radius and surface brightness respectively), we obtain estimates of σ ranging from 90 to $253 \text{ km s}^{-1} \text{ Mpc}^{-1}$, with a mean $168 \pm 40 \text{ km s}^{-1} \text{ Mpc}^{-1}$. Combining these estimates, we obtain $\sigma = 148 \pm 27 \text{ km s}^{-1} \text{ Mpc}^{-1}$, implying $\theta_{\text{crit}} = 0.34 \pm 0.12 \text{ arcsec}$.

The magnification factors of HDF850.1 and HDF850.1K depend strongly on θ_{crit} . Dunlop et al. (2004) argued that the lack of an obvious counterimage to HDF850.1K implies this source must not be far into the strong lensing regime. Neglecting the ellipticity, the singular isothermal sphere (SIS) model predicts an image:counterimage ratio of $(2\theta_{\text{crit}}/\theta) - 1$ for an image-counterimage separation of θ , and a total magnification $2\theta_{\text{crit}}/(\theta - \theta_{\text{crit}})$. This was used to argue that $\theta_{\text{crit}} < 0.35''$ and that the total magnification of HDF850.1K is $\mu < 3.4$. However, the lack of a counterimage can simply be due to the limited sensitivity of the K -band detection. Using the GRAVLENS package (Keeton 2001) we found many SIE configurations consistent with the data that violate these apparent SIS constraints. In particular, an SIE model with $\theta_{\text{crit}} = 0.42''$ places a counterimage within $0.1''$ of the location of a low signal-to-noise feature in the K -band lens-subtracted image. In this model the magnification of HDF850.1K would be $\mu = 4.8$. The same model predicts the submm source HDF850.1 to have a magnification of $\mu \simeq 1.9 \pm 0.3$: at the location of the blue-shifted peak of the [CII] emission in Walter et al. (2012) the magnification is 1.61, while at the red-shifted peak $\mu = 2.12$.

3.2 SED modelling

We performed SED fitting analysis on the detected HST sources 3-586.0 and 3-593.1 (Williams et al. 1996) as a check of the HDF850.1 and HDF850.1K photometry. To perform the multi-wavelength fitting we adopted the popular LePhare package (Arnouts et al. 1999; Ilbert et al. 2006). We use the photometry available from various authors: F300W, F450W, F606W, F814W WFCP2 photometry listed in Fernandez-Soto et al. (1999) and the WIRCam Ks, IRAC 3.6, 4.5, 5.8, $8.0 \mu\text{m}$ photometry reported by Wang et al. (2010). As JH-WFC3 input fluxes we used the values estimated in section 2.2. We then extrapolate from the best fit SED the modelled photometry for each source, convolving our best fit model in each case with the respective filter transmission curve.

These sources have known estimates of redshift: 3-593.1 lies at a photometric redshift of $z = 1.76$ reported by Fernandez-Soto et al. (1998), and 3-856.0, the lens elliptical galaxy, has a spectroscopic redshift of $z = 1.224$ obtained

by Barger et al. (2008); we can thus perform the fit fixing the redshift.

To perform the fit we adopt the extinction law by Calzetti et al. (2000) and we use two different sets of template SED to check the reliability of our fits: the SWIRE templates by Polletta et al. (2007), together with some slightly modified versions from Gruppioni et al. (2010), and the SED obtained by the stellar population synthesis model by Bruzual & Charlot (2003). We found no significant differences between the flux predictions obtained by these two procedures and in table 4 below we report the resulting fluxes obtained using the SWIRE templates. The χ^2 of our best fit SED are low (less than 2). To give an estimate of the uncertainties we should add to our modelled fluxes, we compare our modelled results to the ones measured and given as input, where available. In particular we focus our attention on the range of wavelength around the JH-WFC3 bands which we want to recover completely by our model. In table 4 we thus report the predicted and measured fluxes for the bands of our interest. The difference between the modelled and the measured values are always between 2-5% (depending on the wavelength) and well matched the uncertainties of the input photometry. We thus estimate that this is the uncertainty we should expect to be associated to our JH-WFC3 predicted fluxes. Finally we estimate that the uncertainties coming from the use of a photometric redshift for 3-593.1 is negligible or anyway included in the 5% uncertainties already discussed.

With our photometry of the submm galaxy we are also now able to model the multi-wavelength SED of HDF850.1 and thus make the first constraint on its stellar mass. We use the photometry reported by Cowie et al. 2009 to complete our dataset and we perform the fit following the same approach described above. In the case of HDF850.1 we fit from the NIR to the radio bands and we extrapolate the optical photometry from the best solution. The input bands we used are J, H WFC3, IRAC 5.8 and 8.0 μm (this work), ISO 15 μm (as reported by Downes et al. 1999), MIPS 24, 70 and 160 μm , SCUBA 450 μm , SCUBA 850 μm and IRAM 1.3 (as reported by Cowie et al. 2009). The J, H, 15 μm , 70 μm and 160 μm data are upper limits.

We tried to force the fit to reproduce the Arp 220 as this was the SED claimed to be the best representation of the galaxy in Cowie et al. 2009. We now know that the redshift of the galaxy is $z = 5.183$ rather than the $z = 4.1$ reported in Cowie et al., and we now find that Arp 220 is not able to reproduce the photometry of the galaxy. Instead, we find the best-fit SWIRE template is the ultraluminous starburst galaxy IRAS 20551-4250, shown in Fig. 6. The bolometric luminosity from 8–1000 μm is $1.0 \times 10^{13} L_{\odot}$ (in agreement with the estimate reported by Neri et al. 2014), implying a star formation rate of $1700 M_{\odot}/\text{year}$, with our assumed Salpeter initial mass function from 0.1 – 100 M_{\odot} before magnification correction and using the conversion in Kennicutt 1998 (note that this is a factor of two higher than the estimate in Walter et al. 2012).

To estimate the stellar mass using the SWIRE template SED of IRAS 20551-4250, we calculated the ratio of J -band rest-frame luminosities of HDF850.1 and this local galaxy, and scaled the stellar mass estimate from Mineo et al. (2012) to obtain a stellar mass estimate of $3.4 \times 10^{11} M_{\odot}$, assuming a Salpeter initial mass function from 0.1 – 100 M_{\odot} (not-

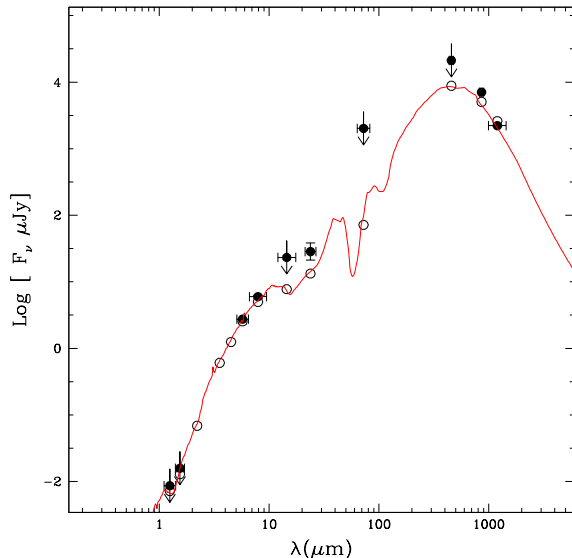


Figure 6. The best fit SED solution of HDF850.1. Solid red line: the best fit SWIRE SED solution corresponding to the IRAS 20551-4250 template from Polletta et al. (2007); full black circles: the input photometry as described in the text; open black circles: the model prediction at each band. The arrows stand for upper limits.

ing that the stellar populations of local galaxies are older than would be found at $z = 5.2$). Alternatively, with the Bruzual & Charlot model, with a Salpeter initial mass function from 0.1 – 100 M_{\odot} (converting the result from Chabrier to Salpeter IMF using the conversion factor described by: $\log M_{\text{Chabrier}} = \log M_{\text{Salpeter}} - 0.24$ as reported in Santini et al. 2014) and a Calzetti extinction law with $E(B - V) = 0.5$, fitting to the 8 μm data and below, we obtain a best fit stellar mass of $1.78 \times 10^{11} M_{\odot}$ and an age of 1.02×10^9 yr. The star formation history of our best fit solution is described by a single stellar population with exponentially decreasing star formation rate and an e-folding timescale of $\tau = 0.3$ Gyr (star formation rate $\propto \exp(-t/\tau)$). Such an age would imply an unphysically high formation redshift; however, there is a degeneracy between the reddening and the age. For $E(B - V) = 0.75$ we obtain an age of 0.6×10^9 yr (formation redshift $z \simeq 10$), and a stellar mass of $2.75 \times 10^{11} M_{\odot}$. Combining all these estimates, and treating the variation between them as an estimate of the uncertainty (random or systematic), we conservatively quote a stellar mass of $(2.5 \pm 1) \times 10^{11} M_{\odot}$ before magnification correction.

4 DISCUSSION: HDF850.1 IN GALAXY SCALING RELATIONS

A “main sequence” that has gained a great deal of popularity is the relationship between total stellar mass M_* and integrated star formation rate¹ $\dot{\rho}_*$ (e.g. Brinchmann et al.

¹ The “main sequence” terminology in this and other galaxy scaling relationships discussed in this paper invites comparisons with the stellar main sequence in the Hertzsprung-Russell diagram, but

Source	Redshift	J/WFC3	H/WFC3	Ks/WIRCAM	3.6 μm	4.5 μm	5.8 μm	8.0 μm
3-586.0	1.22	21.24 / 21.35	20.34 / 20.60	22.87 / 23.15	18.80* / 13.83	16.07* / 11.68	10.32* / 7.39	5.62* / 5.34
3-593.1	1.76	23.62 / 24.16	23.13 / 23.61	26.16 / 26.28	0.97* / 1.04	1.70* / 1.64	4.53* / 2.56	8.45* / 4.49

Table 4. Measured / Predicted JH-WFC3, Ks-WIRCAM total Vega magnitudes and IRAC 1234 total fluxes from the best fit SED of each galaxy. The fluxes are expressed in μJy . The fluxes reported with * are considered as upper limits in the SED fitting.

2004, Daddi et al. 2007, Elbaz et al. 2007, Salim et al. 2007, Zheng et al. 2007, Noeske et al. 2007a,b, Pannella et al. 2009, Daddi et al. 2009, Stark et al. 2009, Peng et al. 2010b, González et al. 2010, Rodighiero et al. 2010, Karim et al. 2011, Rodighiero et al. 2011, Lilly et al. 2013), often expressed in terms of the specific star formation rate $\dot{\rho}_*/M_*$ that is observed to depend only weakly on M_* at a fixed epoch. The total stellar mass is necessarily proportional to the average star formation rate of the galaxy (or its progenitor systems) throughout the age of the Universe at that epoch, so this relationship expresses whether the currently-observed star formation rate is typical of the mean average history of the galaxy.

The age of the Universe at $z = 5.183$ is only 1.1 Gyr, and the specific star formation rate of HDF850.1 is $\dot{\rho}_*/M_* \simeq 8.5 \text{ Gyr}^{-1}$, so HDF850.1 is forming stars at a rate approximately a factor of nine faster than its average up to that point. Rest-frame UV-selected galaxies at this redshift have specific star formation rates in the range $1 - 4 \text{ Gyr}^{-1}$ (Stark et al. 2009, Bouwens et al. 2012, González et al. 2012), so HDF850.1 is also forming stars faster than coeval systems. The galaxies in these samples are also typically less massive ($10^{7-10} M_\odot$), so either HDF850.1 is not representative of lower-mass systems, or star formation at these redshifts is usually episodic (e.g. Stark et al. 2009).

The proximity of HDF850.1K may suggest that a galaxy-galaxy interaction may play a role in HDF850.1's high specific star formation rate. If HDF850.1K were at the same redshift as HDF850.1, then the physical separation between HDF850.1K and the submm galaxy would only be 2.2 kpc, and the pair would be significantly differentially magnified by the $z = 1.22$ elliptical (e.g. Serjeant 2012). However, our constraint on the $H - K$ colour of HDF850.1K of $H - K > 3.8$ strongly suggests that the K -band flux is either contaminated by the foreground lens, or the detection itself is a spurious artefact of the delicate PSF subtraction.

Elbaz et al. (2011) proposed another “main sequence” of galaxies in the polycyclic aromatic hydrocarbon (PAH) luminosity versus bolometric luminosity plane. High- z starbursts curiously resemble scaled-up versions of local star-forming disc galaxies, unlike local ULIRGs which are underluminous in PAH emission for their bolometric luminosities. Like CO $J = 1 - 0$, PAH emission is assumed to be confined to surface layers of GMCs. Variations in the amount of UV shielding by dust are predicted to be responsible for most of the variation in CO abundance in GMCs (e.g. Glover et al. 2010). It may be that a better understanding of the turbulent conditions in the high- z ISM will also shed light on PAH-bolometric luminosity relationship, as well as the

Kennicutt-Schmidt and Elmegreen-Silk relations (see below). It remains to be determined whether the lower PAH abundance in local ULIRGs compared to higher- z ULIRGs is because a larger fraction of PAHs are exposed to hard radiation environments at low- z (e.g. Guhathakurta & Draine 1989), or e.g. because high- z starbursts have more effective PAH replenishment from grain-grain collisions (e.g. Rafikov 2006, Asano et al. 2013) or shocks (e.g. Umana et al. 2010). As with H_2 and other ISM diagnostics, direct detection of PAH emission in HDF850.1 and other $z > 5$ galaxies will have to wait for SPICA or JWST.

HDF850.1 has a molecular gas surface density of $\Sigma_{\text{gas}} = 1.4 \times 10^9 M_\odot \text{ kpc}^{-2}$ (from CO $J = 5 - 4$, and assuming a CO to H_2 conversion of $\alpha_{\text{CO}} = 0.8 M_\odot (\text{K km s}^{-1} \text{ pc}^2)^{-1}$), and a star formation surface density of $\Sigma_{\text{SF}} = 35 M_\odot \text{ yr}^{-1} \text{ kpc}^{-2}$ (Walter et al. 2012), making it typical of high- z merger-driven starbursts on the Kennicutt-Schmidt ($\Sigma_{\text{gas}} - \Sigma_{\text{SF}}$) relation (e.g. Genzel et al. 2010). The fact that the location on this relation appears to be related to specific star formation rate has been used to argue for two discrete modes of star formation in galaxies.

However, before reading too much into the implications for HDF850.1, it is worth reflecting on the physical mechanisms underpinning this relation. The Kennicutt-Schmidt relation is often interpreted in terms of virialised molecular clouds that have, if not a single characterisable size, then at least a well-characterisable average size. In starburst galaxies and major merger systems the assumption of virial equilibrium fails, so one uses a different CO to H_2 conversion. There has been considerable debate as to whether the apparent bimodality in the Kennicutt-Schmidt relation has its origin entirely in the assumed bimodal CO: H_2 conversion (e.g. Genzel et al. 2010, Ivison et al. 2011, Narayanan et al. 2012, Sargent et al. 2013). An alternative to the Kennicutt-Schmidt relation is the Elmegreen-Silk relation, which uses the local dynamical timescale τ_{dyn} to relate Σ_{SF} to $\Sigma_{\text{gas}}/\tau_{\text{dyn}}$. The physical interpretation of this relationship, unlike its Kennicutt-Schmidt counterpart, is to try to characterise how large-scale dynamical processes partly govern the star formation process (e.g. Elmegreen 1997, Silk 1997, Kennicutt & Evans 2012). Again, interpretations often invoke virialised or marginally-bound molecular clouds (e.g. Silk 1997). However, numerical simulations of GMCs in disc galaxies in no way resemble virialised systems. Dobbs & Pringle (2013) find the fraction of gravitationally-bound GMCs to be $< 20\%$ in their simulations; the majority of molecular clouds are unbound. Glover et al. (2010) find the CO and H_2 column densities in GMCs vary by at least two orders of magnitude, and that CO gas abundance does not trace extinction, though H_2 does at least trace the underlying gas distribution. In both sets of simulations there is no clear distinction between “clump” and “inter-clump” mediums; much of the integrated CO luminosity of a galaxy could

note there is no suggestion that galaxies are homologous systems in general, nor that the astrophysics is as well-constrained.

lie in diffuse, low surface brightness regions. It is perhaps only our own optical prejudices that lead us to regard high- A_V regions as distinct entities at all.

The fact that these debates exist even at redshifts $z < 2$ underlines the difficulties in interpreting the $z > 5$ population on these “main sequence” relations, where both observations and modelling are less well constrained. For example, the dependence of α_{CO} on metallicity has only been determined at $z < 2.5$ (Mannucci et al. 2010), and the metallicity of HDF850.1 has not been measured directly. The interpretation of HDF850.1’s location in these global galaxy scaling relations, as with that of any of the highest- z starbursts, must therefore await larger, higher-resolution numerical models to provide better insights into the consequences of observational constraints. The observational situation will improve markedly with direct detections of redshifted H_2 with the SAFARI instrument on SPICA (Roelfsema et al. 2012), and the H_2 would be spatially resolved at sub-kpc scales in high- z starbursts with the proposed FIRI mission (Helmich, Ivison et al. 2007). Spatially resolving the gas and star formation on sub-kpc scales will be strongly diagnostic of the physical processes (e.g. Hopkins, Narayanan & Murray 2013).

5 CONCLUSIONS

The stellar mass of HDF850.1 is $(2.5 \pm 1)\mu^{-1} \times 10^{11} M_\odot$ with a lensing magnification of $\mu \simeq 1.9 \pm 0.3$, implying one of the most extreme specific star formation rates in the galaxy “main sequence” at $z > 5$. The proposed HDF850.1K source is only 2.2 kpc from the submm galaxy in projection, but our $H - K > 3.8$ constraint on the former suggests either its K -band flux is significantly contaminated by the lensing galaxy or the K -band detection itself is an artefact of the delicate subtraction of the foreground lens.

ACKNOWLEDGEMENTS

The authors would like to thank the anonymous referee for helpful comments, and the Science and Technology Facilities Council for support under grant ST/J001597/1. This work is based in part on observations made with the NASA/ESA Hubble Space Telescope, obtained from the data archive at the Space Telescope Science Institute. STScI is operated by the Association of Universities for Research in Astronomy, Inc. under NASA contract NAS 5-26555. This work is also based in part on observations made with the *Spitzer* Space Telescope, which is operated by the Jet Propulsion Laboratory, California Institute of Technology under a contract with NASA.

REFERENCES

Alexander, D.M., et al., 2003, AJ, 126, 539,
 Arnouts, S., et al., 1999, MNRAS, 310, 540
 Asano, R.S., Takeuchi, T.T., Hirashita, H., Nozawa, T., 2013, arXiv:1303.5528
 Aussel, H., Cesarsky, C.J., Elbaz, D., Starck, J.L., 1999, A&A, 342, 313
 Barger, A.J., et al., 1998, Nature, 394, 248
 Barger, A.J., Cowie, L.L., Wang, W.-H., 2008, ApJ, 689, 687

Bouwens, R.J., et al., 2012, ApJ, 753, 83
 Brandt, W.N., et al., 2001, AJ, 122, 2810
 Brinchmann, J., Charlot, S., White, S.D.M., et al., 2004, MNRAS, 351, 1151
 Bruzual, G., Charlot, S., 2003, MNRAS, 344, 1000
 Calzetti, D., et al., 2000, ApJ, 533, 682
 Capak, P., et al., 2004, AJ, 127, 180
 Combes, F., Rex, M., Rawle, T. D., et al. 2012, A&A, 538, L4
 Conselice, C., et al., 2011, MNRAS, 413, 80
 Cowie, L.L., Barger, A.J., Wang, W.-H., Williams, J.P., 2009, ApJ, 697, L122
 Daddi, E., et al., 2007, ApJ, 670, 156
 Daddi, E., et al., 2009, ApJ, 694, 1517
 Dickinson, M., Giavalisco, M., et al., 2003, Proceedings of the ESO Workshop held in Venice, Italy, 24-26 October 2001; eds. R. Bender & A. Renzini, p. 324.
 di Serego Alighieri, S., et al. 2005, A&A, 442, 125
 Dobbs, C.L., Pringle, J.E., 2013, arXiv:1303.4995
 Downes, D., Neri, R., Greve, A., et al. 1999, A&A, 347, 809
 Dunlop, J.S., et al., 2004, MNRAS, 350, 769
 Eales, S.A., et al., 2010, PASP, 122, 499
 Elbaz, D., et al., 2007, A&A, 468, 33
 Elbaz, D., et al., 2011, A&A, 533, A119
 Elmegreen, B.G., 1997, Rev. Mex. A.A. (Serie de Conferencias), 6, 165
 Fernandez-Soto, A., Lanzetta, K.M., Yahil, A., 1999, ApJ, 513, 34
 Frayer, D.T., et al., 2011, ApJL, 726, 22
 Garrett, M.A., de Bruyn, A.G., Giroletti, M., Baan, W.A., Schilizzi, R.T., 2000, A&A, 361, L41
 Gavazzi, R., et al., 2007, ApJ, 667, 176
 Gavazzi, R., et al., 2008, ApJ, 677, 1046
 Genzel, R., et al., 2010, MNRAS, 407, 2091
 Glover, S.C.O., Federrath, C., Mac Low, M.-M., Klessen, R.S., 2010, MNRAS, 404, 2
 González, V., et al., 2010, ApJ, 713, 115
 González, V., et al., 2012, arXiv:1208.4362
 Griffin, M.J., et al., 2010, A&A, 518, L3
 Grogin, N.A., et al., 2011, ApJS, 197, 35
 Gruppioni, C., Pozzi, F., Andreani, P., et al. 2010, A&A, 518, L27
 Guhathakurta, P., & Draine, B.T. 1989, ApJ, 345, 230
 Guidetti, D., et al., 2013, MNRAS, 432, 2798
 Heiderman, A. Evans, N.J. II, Allen, L.E., Huard, T., Heyer, M., 2010, ApJ, 723, 1019
 Helmich, F.P., Ivison, R.J., et al., 2007, arXiv:0707.1822
 Hogg, D.W., et al., 1997, AJ, 113, 474
 Holden, B.P., et al., 2005, ApJ, 620, L83
 Hopkins, P.F., Narayanan, D., Murray, N., 2013, arXiv:1303.0285
 Hughes, D.H., et al., 1998, Nature 394, 241
 Ilbert, O., et al., 2006, A&A, 457, 841
 Ivison, R.J., et al., 2011, MNRAS, 412, 1913
 Karim, A., et al., 2011, ApJ, 730, 61
 Kennicutt, R.C., 1998, ApJ, 498, 541
 Kennicutt, R.C., Evans, N.J. II, 2012, ARA&A, 50, 531
 Koekemoer, A.M., ApJS, 197, 36K=
 Krist, J.E., Hook, R.N., Stoehr, F., 2011, Proc. SPIE, 8127, 81270J
 Lilly, S.J., Carollo, C.M., Pipino, A., Renzini, A., Peng, Y., 2013, ApJ, in press (arXiv:1303.5059)
 Lupu, R.E., et al. 2012, ApJ, 757, 135
 Mannucci, F., Cresci, G., Maiolino, R. Marconi, A., Gnerucci, A., 2010, MNRAS, 408, 1195
 Mineo, S., Gilfanov, M., Sunyaev, R., 2012, MNRAS submitted (arXiv:1207.2157)
 Morrison, G.E., Owen, F.N., Dickinson, M., Ivison, R.J., Ibar, E., 2010, ApJS, 188, 178
 Murray, N., 2011, ApJ, 729, 133
 Narayanan, D., Bothwell, M., Davé, R., 2012, MNRAS, 426, 1178
 Negrello, M., et al., 2010, Science, 330, 800

- Neri, R., Downes, D., Cox, P., & Walter, F. 2014, A&A, in press (arXiv:1401.2396)
- Noeske, K.G., et al., 2007a, ApJ, 660, L43
- Noeske, K.G., et al., 2007b, ApJ, 660, L47
- Oliver, S.J., et al., 2012, MNRAS, 424, 1614
- Pannella, M., et al., 2009, ApJ, 698, L116
- Peng, C.Y., Ho, L.C., Impey, C.D., Rix, H.-W., 2010a, AJ, 139, 2097
- Peng, Y., et al., 2010b, ApJ, 721, 193
- Pineda, J.L., Goldsmith, P.F., Chapman, N., Snell, R.L., Li, D., Cambr esy, L., Brunt, C., 2010, ApJ, 721, 686
- Polletta, M., et al. 2007, ApJ, 663, 81
- Pope, A., & Chary, R.-R., 2010, ApJ, 715, L171
- Rafikov, R.R., 2006, ApJ, 646, 288
- Riechers, D. A., Bradford, C. M., Clements, D. L., et al. 2013, Nature, 496, 329
- Rodighiero, G., et al., 2010, A&A, 518, L25
- Rodighiero, G., et al., 2011, ApJ, 739, L40
- Salim, S., et al., 2007, ApJS, 173, 267
- Santini, P., Maiolino, R., Magnelli, B., et al. 2014, A&A, 562, A30
- Sargent, M.T., et al., 2013, ApJ submitted (arXiv:1303.4392)
- Serjeant S., et al., 1997, MNRAS, 289, 457
- Serjeant, S., 2012, MNRAS, 424, 2429
- Silk, J., 1997, ApJ, 481, 703
- Smail, I., et al., 1997, ApJL, 490, L5
- Solomon, P.M., Rivolo, A.R., Barret, J., Yahil, A., 1987, ApJ, 319, 730
- Stark, D.P., et al., 2009, ApJ, 697, 1493
- Swinbank, A.M., et al., 2010, Nature, 464, 733
- Teplitz, H.I., et al., 2011, AJ, 141, 1
- Teplitz, H.I., et al., 2013, AJ, 146, 159
- Umana, G., Buemi, C.S., Trigillo, C., Leto, P., Hora, J.L., 2010, ApJ, 718, 1036
- Walter, F., et al., 2012, Nature, 486, 233
- Wang, W.-H., Cowie, L. L., Barger, A. J., Keenan, R. C., & Ting, H.-C. 2010, ApJS, 187, 251
- Williams, R.E., et al., 1996, AJ, 112, 1335
- Zheng, X.Z., et al., 2007, ApJ, 661, L41